PAPER

Check for updates

UV-Vis spectrophotometry of quinone flow battery electrolyte for *in situ* monitoring and improved electrochemical modeling of potential and quinhydrone formation†

Liuchuan Tong, [ID] ‡[a] Qing Chen, [ID] ‡§[b] Andrew A. Wong, [ID] ‡[b]
Rafael Gómez-Bombarelli, [ID] ¶[a] Alán Aspuru-Guzik [ID] [a] Roy G. Gordon [ID] [a] and
Michael J. Aziz [ID] *[b]

Quinone-based aqueous flow batteries provide a potential opportunity for large-scale, low-cost energy storage due to their composition from earth abundant elements, high aqueous solubility, reversible redox kinetics and their chemical tunability such as reduction potential. In an operating flow battery utilizing 9,10-anthraquinone-2,7-disulfonic acid, the aggregation of an oxidized quinone and a reduced hydroquinone to form a quinhydrone dimer causes significant variations from ideal solution behavior and of optical absorption from the Beer–Lambert law. We utilize *in situ* UV-Vis spectrophotometry to establish (a), quinone, hydroquinone and quinhydrone molar attenuation profiles and (b), an equilibrium constant for formation of the quinhydrone dimer (K_{QHQ}) $\sim$ 80 M^{-1}. We use the molar optical attenuation profiles to identify the total molecular concentration and state of charge at arbitrary mixtures of quinone and hydroquinone. We report density functional theory calculations to support the quinhydrone UV-Vis measurements and to provide insight into the dimerization conformations. We instrument a quinone–bromine flow battery with a Pd–H reference electrode in order to demonstrate how complexation in both the negative (quinone) and positive (bromine) electrolytes directly impacts measured half-cell and full-cell voltages. This work shows how accounting for electrolyte complexation improves the accuracy of electrochemical modeling of flow battery electrolytes.

Introduction

Quinones are widely involved in many processes involving electron transfer, such as ubiquinone in respiratory systems[1] and plastoquinone in photosynthesis.[2] Their unique electrochemical properties attract much attention from electrochemists who often study quinones as model systems for spontaneous proton-coupled electron transfer processes.[3] In addition, because of their high aqueous solubility, fast charge-transfer kinetics and the capability of multi-electron transfer in addition to being composed of earth abundant elements, quinones have been the

subject of increased attention in the field of electrical energy storage. Quinones in their crystalline or polymeric solid forms find use as reactive electrodes,[4,5] and solvated quinone molecules are employed in aqueous and non-aqueous redox flow batteries.[6–9]

Recent works explore low-cost electrolytes containing redox-active quinone molecules for aqueous flow batteries. Anthraquinones have been rendered highly soluble in acidic and basic solutions through sulfonation[6] and hydroxylation[10] respectively, and the low redox potentials of certain anthraquinones yield a considerable cell voltage when paired with a high potential redox couple.[10] Quinone-based flow batteries have attracted a great deal of attention for their potential to regulate fluctuations in energy demand and the address the intermittency challenge of renewable wind and photovoltaic supply through cost-effective grid-scale storage.[6,10,11]

To further improve quinone-based flow battery performance, the behavior of the quinone/hydroquinone redox couple must be understood, especially at the high concentration required for practical operation. Quinone molecules are known to form quinhydrone complexes between the oxidized and the reduced forms.[12–14] This dimer arises from hydrogen bonding, charge-transfer between quinone and hydroquinone, and from a

[a] Department of Chemistry and Chemical Biology, Harvard University,
12 Oxford Street, Cambridge, Massachusetts 02138, USA
[b] Harvard School of Engineering and Applied Sciences, 29 Oxford Street,
Cambridge, Massachusetts 02138, USA. E-mail: maziz@harvard.edu
† Electronic supplementary information (ESI) available. See DOI: 10.1039/c7cp05881k
‡ These authors contributed equally as co-first authors.
§ Present address: Department of Mechanical and Aerospace Engineering, Hong Kong University of Science and Technology, Clear Water Bay, Kowloon, Hong Kong.
¶ Present address: Kyulux North America Inc., 10 Post office Sq. Boston, Massachusetts, 02109, USA.

31684 | *Phys. Chem. Chem. Phys.,* 2017, **19**, 31684–31691

This journal is © the Owner Societies 2017

combination of dispersion interactions between the extended aromatic systems when they coexist in the solution. Such a dimer structure was used in the invention of quinhydrone pH electrodes almost a century ago.[15] This quinhydrone has its own unique optical absorbance signature due to allowed inter-molecular electron transfer. The interaction of dissolved monomers results in a change in the electrolyte activity, shifting the reduction potential. When the speciation is greatly driven toward quinhydrone formation, the cell voltage can significantly deviate from that of an ideal solution, in large part due to changes in the unbound monomer species concentrations; this is similar to the behavior of the positive side of the QBFB where the tribromide complex dominates the speciation.

In this work, we use UV-Vis absorption spectrophotometry and density functional theory (DFT) calculations to quantify the optical properties of quinone, hydroquinone and quinhydrone. Additionally, we explore the underlying quinhydrone formation mechanism, based on which we estimate a value for the quinhydrone equilibrium constant. UV-Vis spectrophotometry has already been established as a valuable tool for those interested in operating commercial flow batteries.[16,17] By considering quinhydrone formation as well as complexation in the bromine-based positive electrolyte, full-cell and half-cell voltage approximations using the unbound monomer species concentrations applied to the Nernst equation are significantly improved, matching experimentally measured values.

Experimental

In this study, the quinone used is specifically 9,10-anthraquinone-2,7-disulfonic acid (AQDS). For conciseness in the following discussion, quinone (Q), hydroquinone (HQ) and quinhydrone (QHQ) will stand for AQDS, H_2AQDS, and their quinhydrone dimer respectively.

In-line UV-Vis spectrophotometry

All reported UV-Vis spectrophotometry data in this study are collected in-line during electrochemical experiments with a custom-built 5 cm^2 quinone–hydrogen flow cell (QHFC), as shown schematically in Fig. 1(a). Hydrogen is used at the charging anode made of platinum-coated porous carbon paper, separated by a Nafion 212 ion exchange membrane. Hydrogen is used specifically to prevent crossover contamination in the quinone electrolyte from other redox species. A 100 μm optical path-length flow cell (Ocean Optics FIA-USP-100) is plumbed to the outlet of the QHFC. A deuterium–tungsten light source (Ocean Optics DH-2000-BAL) is connected to the optical flow cell using 25 cm optical fibers (Ocean Optics QP400-025-SR-BX) with a mirroring optical fiber and UV-Vis spectrophotometer (Ocean Optics Flame-S-UV-VIS). This setup is used for all absorption measurements. 20 mL of 200 mM AQDS in 1 M H_2SO_4 electrolyte is pumped through the QHFC at 60 mL min^{-1} with a peristaltic pump (Cole Parmer MasterFlex L/S). Given an open-circuit voltage (OCV) of 0.213 V, chronoamperometry at −0.1 V is used to fully reduce the flowing quinone in the carbon electrode while the UV-Vis absorption spectra are being recorded every 5 seconds. The quinone is then re-oxidized by chronoamperometry at 0.5 V, generating hydrogen cathodically at the hydrogen electrode. 10 mL of quinone electrolyte is then removed and replaced by 10 mL of 1 M H_2SO_4; a portion of the removed electrolyte is saved to accurately quantify the concentration in each experiment. The electrochemical procedure and subsequent dilution are repeated to obtain spectra at various concentrations. The starting quinone concentration, taken at 0% state of charge (SOC), for each experiment is defined as $[Q]_0$.

The chronoamperometry charge–discharge data are normalized by coulometry from 0% to 100% SOC to identify spectra in 10% SOC increments. SOC is defined by the fraction of total hydroquinone molecule concentration ($[HQ] + [QHQ]$) and the starting quinone concentration (i.e. ($[HQ] + [QHQ])/[Q]_0$). The 0% and 100% SOC absorbance spectra for each starting concentration are then normalized by that concentration and the optical flow cell path length to give the molar attenuation of the quinone and hydroquinone respectively. As will be shown later, the spectra at intermediate SOCs can be determined by a linear system of equations using these molar attenuation spectra.
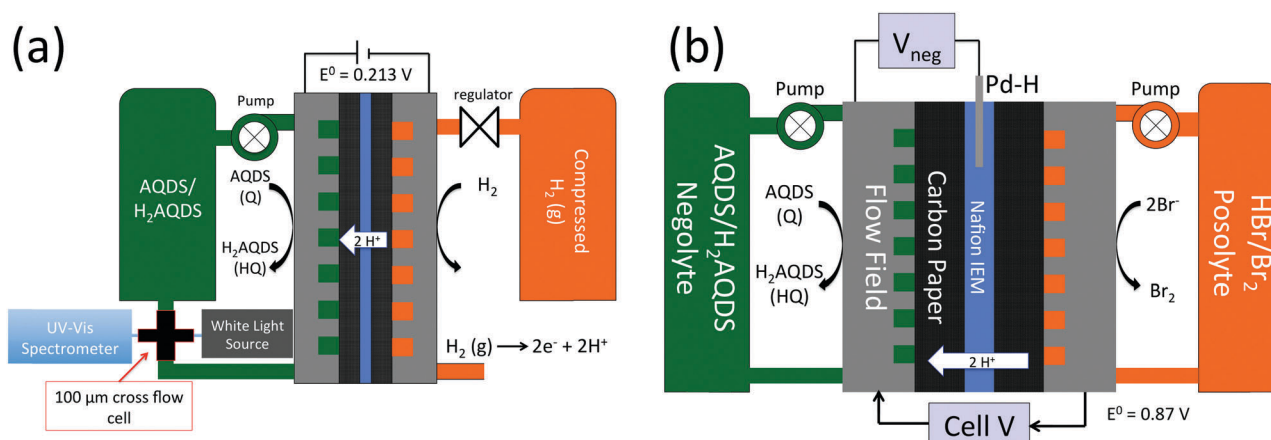

Fig. 1 Cell configuration for (a) quinone–hydrogen flow cell (QHFC) and (b) quinone–bromine flow battery (QBFB).

This journal is © the Owner Societies 2017

Phys. Chem. Chem. Phys., 2017, 19, 31684–31691 | 31685

UV-Vis spectra taken between 0% and 100% SOC at several different concentrations demonstrate the appearance, only at intermediate states of charge, of an absorbance peak between 500 nm and 800 nm, *i.e.* at significantly longer wavelengths than the quinone and hydroquinone absorption ranges alone. These spectra are fit across this wavelength range to obtain a quinhydrone equilibrium constant (K_{QHQ}) and a molar attenuation constant ($\varepsilon_{QHQ}(\lambda)$).

Theoretical

The interaction between reduced and oxidized AQDS is modeled using DFT. Initial conformations are generated stochastically using frozen monomer geometries and varying the relative displacement and orientation of the reduced and oxidized molecules. These starting configurations are pre-optimized using the PM6DH, a computationally-fast semi-empirical method with corrections for dispersion and hydrogen bond interactions. The geometries are further refined by optimizing the geometries at the DFT B3LYP/6-31G(d) level of theory[18] with an additive D3 dispersion interaction correction[19] using Terachem v1.5. Single point calculations at the optimized geometries are performed using B3LYP-D3/6-311G(d,p) to estimate aggregation energies, and using TD-DFT B3LYP-D3/6-31G(d) and TD-DFT ωB97X-D/6-31G(d) levels of theory[20] to estimate the absorption spectra of the quinhydrone. Solvent effects are included in the DFT calculations using the conductor-like polarizable continuum (CPCM) solvation model in water.[21,22]

In order to capture the role of interaction with the water solvent molecules, calculations are also performed on explicitly hydrated complexes *via* cluster-continuum calculations.[23] One water molecule is added per hydrogen-bond donor atom (oxygen atoms), for a total of 16 water molecules. Solvent molecules are placed randomly near oxygen atoms in the pre-arranged quinhydrone system and then relaxed by full geometry optimization.

Electrochemistry

Because the negolyte, posolyte (negative and positive electrolyte respectively) and overall cell voltages (E_{neg}, E_{pos}, and E_{cell} respectively) will change based on the true electrolyte species concentrations, we use electrochemical techniques to corroborate the K_{QHQ} value measured by UV-Vis spectrophotometry. To extract the E_{neg} and E_{pos} experimentally, we install a reference electrode in the quinone–bromine flow battery (QBFB) to separate the two half-cell voltage contributions from the total cell voltage. The cell configuration for this half-cell experiment is illustrated in Fig. 1(b). A Pd–H reference electrode is sandwiched between two sheets of Nafion membrane, the location of which is justified by prior research.[24] All potentials are reported here *vs.* SHE based on an average potential of the Pd–H electrode measured before and after the half-cell testing. Under these conditions, the reference electrode potential is ~50 mV *vs.* RHE.[25] A less than 5 mV potential change is usually observed during the measurement.

The build of the quinone–bromide cell follows that in ref. 25 (Chen *et al.*). On each side, a commercial graphite plate with interdigitated flow channels (Fuel Cell Tech, Albuquerque, NM)

feeds an electrolyte to a porous carbon electrode at a rate of 100 mL per minute controlled by a MasterFlex (Cole Parmer) diaphragm pump. The electrode comprises a stack of 3 sheets of SGL 10AA (each nominally 400 μm thick) carbon paper, compressed to ~75% of the original thickness, defined by Teflon gaskets. The geometric area of the electrodes is 2 cm^2. The SGL paper is pre-treated by baking at 400 °C in air for 24 hours. The reference electrode is sandwiched between two Nafion 115 membranes, which are soaked in DI-water at room temperature for ~24 hours prior to the experiments. The temperature of the cell is approximately 20 °C.

15 to 20 mL of negolyte is used for the cell. It contains either 1.0 or 0.2 M AQDS, with an additional 1.0 M or 2.6 M H_2SO_4 respectively to maintain 3 M free protons in the electrolyte. The posolyte contains 0.5 M Br_2 and 3.0 M HBr. The volume ratio is maintained at 1:1.2 negolyte:posolyte. For each cell, the charge associated to the reduction of AQDS is assessed by reducing the negolyte at −0.1 V *vs.* Pd–H, until the current reaches a steadily low value (as demonstrated in Fig. S6, ESI†). With this assessment of the total charge, the quinone is reduced in 10% SOC increments between 0% and 100% and the open circuit voltage with respect to the reference electrode is measured at each increment. These data are compared to theoretical potentials based on the Nernst equation based on the unbound monomer species concentrations both omitting and incorporating the effect of species complexation.

Results and discussion

In-line UV-Vis spectrophotometry

In an operating quinone flow battery, the SOC relates the relative concentrations of Q and HQ species and is most often determined by electrochemical methods. *in situ* UV-V is spectrophotometry measurements of Q and HQ species at different SOCs can be found in Fig. 2(a). Normalizing the absorption optical density (OD) at 0% and 100% SOC by the flow cell path length (100 μm) and solution concentration (2.25 mM) provides the active species molar attenuation ($\varepsilon(\lambda)$). Fig. 2(b) shows the molar attenuation of the quinone $\varepsilon_Q(\lambda)$ and hydroquinone $\varepsilon_{HQ}(\lambda)$ in the UV and visible regions. Using the Beer–Lambert law,

$$A(\lambda) = \varepsilon(\lambda)c\,l \tag{1}$$

where A is the absorbance ($-\log(\text{transmittance})$) of the solution, c is the concentration, and l is the optical path length through the solution, the absorbance spectrum for $\lambda < 500$ nm at an intermediate state of charge can be determined by a linear combination between Q and HQ:

$$A(\lambda) = \varepsilon_Q(\lambda)[Q]_0 l(1 - \text{SOC}) + \text{SOC}\,\varepsilon_{HQ}(\lambda)[Q]_0 l \tag{2}$$

As will be shown later, the dimerization product of Q and HQ is the only species that absorbs in the region $\lambda > 500$ nm. Fig. 2(c) shows that the intermediate-SOC solution absorption average for various starting solution concentrations can be recreated by a linear combination between Q and HQ absorbance between
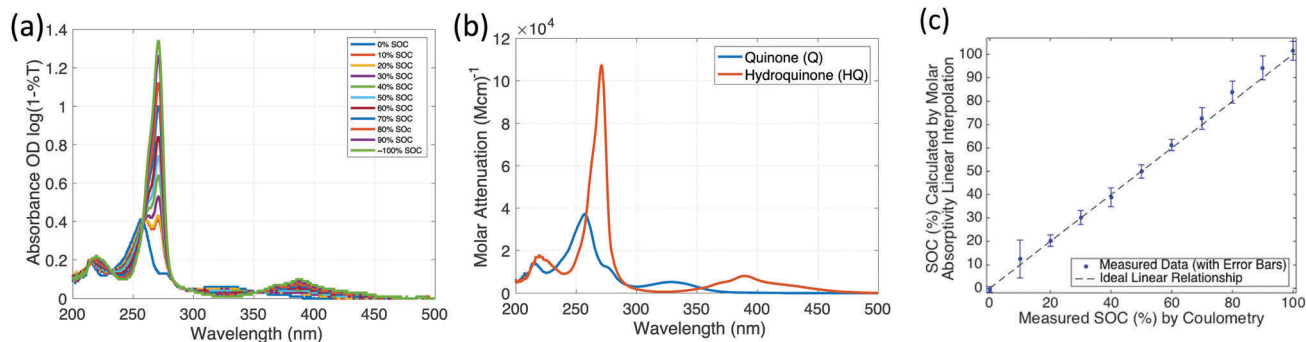
31686 | *Phys. Chem. Chem. Phys.*, 2017, **19**, 31684–31691

This journal is © the Owner Societies 2017

Fig. 2 (a) *In situ* UV-Vis absorbance spectra by state of charge (SOC) for 1.25 mM AQDS through a 100 µm optical flow cell. (b) UV molar attenuation spectra for quinone ($\varepsilon_Q(\lambda)$) and hydroquinone ($\varepsilon_{HQ}(\lambda)$). (c) Quinone SOC calculated by a linear combination of Q and HQ molar attenuation *vs.* SOC measured by coulometry showing a close relationship between the two techniques. Data points are averaged from various dilute AQDS concentrations between 1 and 56 mM. All data are measured using a 100 um path length flow cell as shown in Fig. 1(a). The average values are reported with error bars representing one standard deviation. Attenuation values above 1.6 OD are considered to reach a photon-detection limit for the spectrometer and are not used when calculating the average.

200–500 nm wavelength using the SOC as the only fitting parameter. This method, using $[Q]_0$ as an additional fitting parameter, can be used to identify the concentration and the SOC of a quinone flow battery *in operando*, providing a non-electrochemical method for measuring these quantities.

Quinhydrone

It has been known that Q and HQ dimerize to quinhydrone (QHQ), a phenomenon that is detectable at sufficiently high concentrations of both parent species. The first step toward understanding the impact from quinhydrone formation is quantifying the reaction equilibrium constant. The quinhydrone equilibrium can be written as

$$Q + HQ \overset{K_{QHQ}}{\longleftrightarrow} QHQ \tag{3}$$

with equilibrium constant K_{QHQ} defined as

$$K_{QHQ} = \frac{\gamma_{QHQ}[QHQ]}{\gamma_Q[Q]\gamma_{HQ}[HQ]} \tag{4}$$

where γ represents the molar activity coefficient of a particular species and the square brackets indicate concentrations in moles per liter. We can further define an activity-coefficient corrected equilibrium constant K_{QHQ}' as

$$K_{QHQ}' = K_{QHQ}'/\gamma' = \frac{[QHQ]}{[Q][HQ]} \tag{5}$$

in which $\gamma' = \gamma_{QHQ}/\gamma_Q\gamma_{HQ}$.

Instantaneous $[Q]$, $[HQ]$ and $[QHQ]$ in the solution can be connected to $[Q]_0$ *via* cell SOC in the form of

$$[Q]_0 = [Q] + [HQ] + 2[QHQ], \tag{6}$$

$$SOC = \frac{[HQ] + [QHQ]}{[Q] + [HQ] + 2[QHQ]} = \frac{[HQ] + [QHQ]}{[Q]_0} \tag{7}$$

K_{QHQ}' can therefore be expressed as a function of $[Q]_0$, $[QHQ]$ and SOC

$$K_{QHQ}' = \frac{[QHQ]}{[Q]_0^2 SOC(1 - SOC) - [Q]_0[QHQ] + [QHQ]^2} \tag{8}$$

With known $[Q]_0$ and SOC, K_{QHQ}' may be determined from a measurement of $[QHQ]$.

Given the distinct light absorption spectra of Q and HQ as described above, it is possible to quantify deviations from an ideal spectrum. At intermediate SOCs a broad absorbance band between 550 and 800 nm arises, showing no proportionality to either $[Q]$ or $[HQ]$, as shown in Fig. 3(a). This absorbance reaches maximum at 50% SOC or a 1:1 stoichiometry between Q and HQ and is symmetric by SOC about this point. This result indicates that the species absorbing in this band is correlated to the product of the concentrations of Q and HQ, as would be expected for a QHQ complex.

$[QHQ]$ is then quantified based on the measured spectra at intermediate SOCs for several different starting quinone concentrations. For the visible wavelengths over which Q and HQ do not absorb (*i.e.* >550 nm), the absorbance of QHQ can also be given by the Beer–Lambert law

$$A_{QHQ}(\lambda) = \varepsilon_{QHQ}(\lambda)[QHQ]l \tag{9}$$

where ε_{QHQ} is the QHQ molar attenuation coefficient. Combining eqn (8) and (9) gives

$$[Q]_0^2 SOC(1 - SOC) = \left(\frac{1}{K_{QHQ}'} + [Q]_0\right)\frac{A_{QHQ}(\lambda)}{\varepsilon_{QHQ}(\lambda)l} - \left(\frac{A_{QHQ}(\lambda)}{\varepsilon_{QHQ}(\lambda)l}\right)^2 \tag{10}$$

From the experimental setup, $[Q]_0$, SOC and l are known and $A_{QHQ}(\lambda)$ is measured. Allowing K_{QHQ}' and $\varepsilon_{QHQ}(\lambda)$ to be independent variables, we fit the data to obtain a wavelength-dependent QHQ molar attenuation, as shown in Fig. 3(b). The result is $K_{QHQ}' \sim 80$ M^{-1}, which can be modeled across all SOCs and fits well to experimental data as shown in Fig. 3(c). Later in this work, this value of the equilibrium constant will be used to better account for the negolyte half-cell potential.

Quantum chemical calculations

DFT calculations are performed to support the experimentally observed quinhydrone absorbance as well as to gain insight
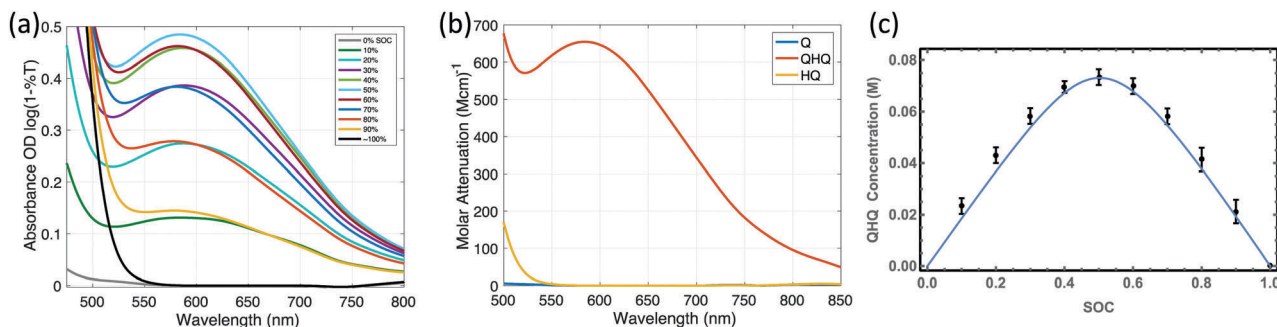
Fig. 3 (a) Visible absorbance spectrum of quinone electrolyte ($[Q]_0$ = 209 mM) at different states of charge. At 0% and 100% SOC between 550 nm and 800 nm, the Q and HQ absorbance spectra are 0, but the QHQ absorbance persists at intermediate states of charge. (b) Quinhydrone molar attenuation ($\varepsilon_{QHQ}(\lambda)$). (c) Concentration profiles of QHQ *vs.* SOC at $[Q]_0$ = 209 mM. Black dots are the measured optical absorbance between 600–610 nm wavelength divided by the molar attenuation coefficient and the optical path length. The blue line is the expected quinhydrone concentration given K_{QHQ} = 80 M^{-1}.

into the quinhydrone formation mechanism. B3LYP-D3/6-31G* geometry optimizations are carried out for over one hundred stochastic quinhydrone configurations after pre-optimization with the semiempirical method PM6DH.

Water molecules are known to interact strongly with solutes *via* their large electric dipole and also by forming hydrogen bonds with the solute. These direct interaction models are usually improved through inclusion of explicit water molecules. However, the strong water–water interactions tend to distort the energetics of the system, especially in the case of weakly bonded systems like quinhydrone. We compare the results for our two approaches below.

The –SO$_3$H moieties in Q and HQ are modeled as the protonated acid despite their high acidity (p$K_a \sim -2$), because of the strong ionic interactions between hydronium ions and ionized sulfonates. This approach has been shown to produce more exact results when calculating molecular properties such as reduction potential of sulfonated quinones.[26] In addition, the increased degrees of freedom of the position of the counter-ions, makes the exploration of this parameter space computationally expensive.

The modeling results show that quinhydrone dimers converged to two types of arrangements—stacked or oblique, as shown in Fig. 4(b) and (c). In the stacked dimer, the major axes of the two anthraquinone rings are aligned and the sulphonic acid groups point in opposite directions. In the oblique one, the axes of the two anthraquinone rings form an angle of 25–45 degrees and the sulfonic acid groups point in the same direction and are interlocked. The distances between the centers of mass of AQDS (Q) and H$_2$AQDS (HQ) in the stacked and oblique anhydrous configurations are 3.35 Å and 3.63 Å respectively, which is around twice the van der Waals' radius for carbon (1.7 Å). Both anhydrous configurations show significant hydrogen bonding between quinone and hydroquinone, despite the large distance between groups and the unfavorable orientation. There are also appreciable interactions between sulfonic groups and the quinone hydroxyls. In the explicitly-solvated molecules these hydrogen bonds within the dimer tend to be disrupted, but the relative orientations and the stacking distances do not change significantly.
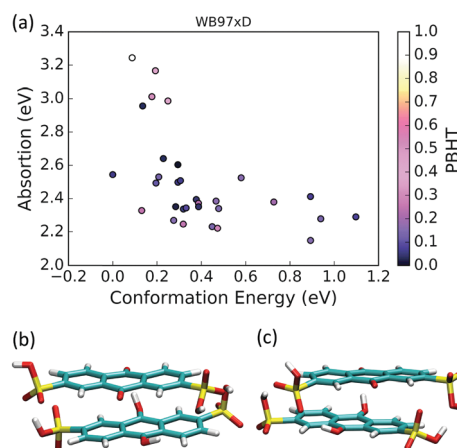

Fig. 4 (a) Interdependency among absorption energy, energy for molecular conformations and orbital overlap for locally optimal configuration. Color scale indicates PBHT overlap. (b) Stacked and (c) oblique quinhydrone dimer geometries.

UV-Vis spectra are predicted for all the configurations. The long-range corrected ωB97X-D functional is applied, as it includes a correction to the DFT exchange in order to better describe charge-transfer states. Fig. 4(a) shows the correlation between absorption energy, relative energy of the configuration, and the degree of charge transfer, estimated as the PBHT overlap.[27] This parameter gives an estimate of the overlap between the starting and final orbitals of an optical transition; a value of 1 means maximum overlap, and 0 corresponds to null overlap (large degree of charge transfer). As shown in this figure, charge-transfer excitations from reduced to oxidized are lower energy and show little orbital overlap (dark points), whereas localized excitations in the monomers (high overlap, bright points) tend to occur at much higher energies, in the UV region of the spectrum.

Table 1 compares the prediction for the absorption maximum and the oscillator strength of the quinhydrone optical transition. The experimental oscillator strength is obtained by deconvolving the quinhydrone absorption spectrum to a sum of

31688 | *Phys. Chem. Chem. Phys.*, 2017, **19**, 31684–31691

This journal is © the Owner Societies 2017

Table 1 Predicted and measured optical properties, predicted absorption energies (E_{abs}) and oscillator strength (f)

Solvent	ω-B97XD/6-31G(d)		Experimental
	Implicit	Explicit	
E_{abs} (eV)	2.27	1.81	2.11
f	0.05	0.05	0.002

Fig. 5 (a) Q, HQ and QHQ concentrations with 0.2 M $[Q]_0$ vs. SOC. (b) Half-cell voltage vs. SOC. Black dots are experimental data measured in the AQDS-bromide cell, Fig. 1(b), orange and blue lines are the calculated values of E_{neg} with and without considering QHQ formation with K_{QHQ} = 80 M^{-1}, respectively.

Gaussians and fitting the charge-transfer absorption peak. The predicted absorption energies (E_{abs}) are in good agreement with experiments, particularly in implicit solvent (+0.16 and −0.30 eV deviation for implicit and explicit solvent, respectively). The low oscillator strength (f) and PBHT overlap (Fig. 4(a)) confirm the large charge-transfer character of the optical transition between the reduced hydroquinone HOMO and the oxidized quinone LUMO.

Quinone electrochemistry

The quinhydrone complexation can be used to improve the predictive capability of the analytical half- and full-cell potential. Quinone speciation affects its redox potential, which is also the negative terminal potential in the quinone–bromine flow battery (QBFB), through the Nernst equation as

$$E_{neg} = E_Q^0 + \frac{RT}{nF}\ln\left(\frac{a_Q a_{H^+}^2}{a_{HQ}}\right) = E_Q^{0\prime} + \frac{RT}{nF}\ln\left(\frac{[Q]\left[H_{neg}^+\right]^2}{[HQ]}\right)$$

(11)

$$E_Q^{0\prime} = E_Q^0 + \frac{RT}{nF}\ln\left(\frac{\gamma_Q \gamma_{H^+}^2}{\gamma_{HQ}}\right)$$

(12)

where E_Q^0 is the standard potential (0.213 V vs. SHE) and $E_Q^{0\prime}$ is the formal potential of the Q/HQ redox couple, a_i and γ_i are the activities and molar activity coefficients respectively of each species and are functions of the species concentrations (e.g. [Q]). R is the universal gas constant, T is the temperature (300 K), n is the electron transfer number (two), F is Faraday's constant (96 485 C mol^{-1}), and $[H_{neg}^+]$ is the free proton concentration in the negolyte, which is maintained at 3 M by protons from the quinone species and additional sulfuric acid. The formal potential, defined by the measured negative half-cell potential when [Q] = [HQ], is 0.219 ± 0.016 V and is closely approximated by the quinone standard potential. This results in $\gamma' = \gamma_{QHQ}/\gamma_Q\gamma_{HQ} \sim 1$, leading to the approximation $K_{QHQ}' = K_{QHQ}$. [Q] and [HQ] can be numerically derived from eqn (6)–(8) with K_{QHQ} = 80 M^{-1} from the analysis of the UV-Vis spectrophotometry measurements. The concentration vs. SOC of each of these three species at $[Q]_0$ = 0.2 M is shown in Fig. 5(a).

The measured E_{neg} vs. SOC at $[Q]_0$ =0.2 M is plotted as black dots in Fig. 5(b). Calculated E_{neg} values based on eqn (11) are plotted as solid lines. The blue curve in Fig. 5(b) assumes no quinhydrone formation and shows a steep voltage ascent or descent close to 0% and 100% SOC but little voltage variation in the remaining SOC region. This contrasts sharply with the
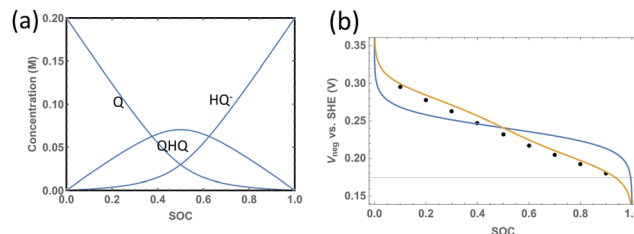
measured result. The orange line instead uses the [Q] and [HQ] values shown in Fig. 5(a) applied to eqn (11). The greatly improved agreement between the measured E_{neg}, the orange line indicates that the Q/HQ redox potential is significantly influenced by the formation of QHQ.

High concentration quinone activity

To increase energy- and power-density, practical flow batteries incorporate active electrolytes closer to their solubility limits, e.g. 1.0 M AQDS (2.0 M electrons). Fig. 6(a) shows the calculated QHQ dimer aggregation between 0% and 100% SOC at $[Q]_0$ = 1.0 M again with K_{QHQ} = 80 M^{-1}. Fig. 6(b) shows the measured E_{neg} vs. SOC for this solution compared to the calculated potential from eqn (11) with (orange line) and without (blue line) accounting for the QHQ formation. It is evident that at this concentration, including QHQ overcorrects the negative electrode potential. This is because the activity of concentrated electrolyte solutions can often be influenced by higher order molecular interactions. This additional deviation from the unbound monomer species concentration-corrected ideal solution behavior leads to small but appreciable changes in electrochemical potential; because of this the activity coefficients, γ, again become important. For example, whereas the orange line in Fig. 6(b) shows the calculated E_{neg} vs. SOC assuming that γ' is invariant, the green line in Fig. 6(b) shows the calculated E_{neg} vs. SOC with the arbitrary assumption that γ' varies exponentially from $\frac{1}{4}$ to 4 as the SOC
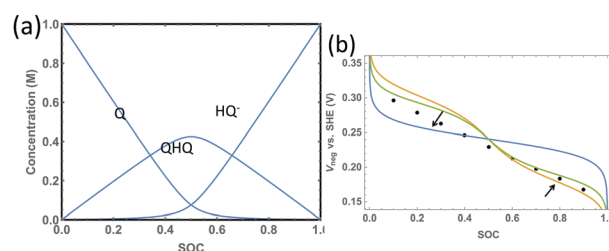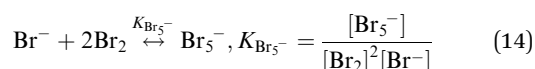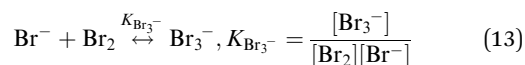

Fig. 6 (a) Q, HQ and QHQ concentrations with 1.0 M $[Q]_0$ vs. SOC. (b) Half-cell voltage vs. SOC. Black dots are experimental data measured in the AQDS-Bromide cell, Fig. 1(b), orange and blue lines are the calculated E_{neg} with and without considering QHQ formation with K_{QHQ} = 80 M^{-1}, respectively. The green line and arrows show how incorporating changes to the Q and HQ activity coefficients can improve the approximation of the negative half-cell potential as discussed in the text.

varies from 0% to 100%. As shown in the next section, solutions to the full-cell open circuit potential incorporating the QHQ formation only, with γ' invariant, are sufficient for significantly improving the accuracy of the calculation. Observations for the high-concentration change in activity are discussed in the ESI;† a full resolution will require further research.

Bromine electrochemistry

The above results show that the consideration of the quin-hydrone equilibrium indeed improves the voltage prediction of the negative side of the QBFB. To develop a complete voltage prediction for the QBFB, we need to further include the equilibrium between bromine and bromide in the posolyte. The formation of tribromide and pentabromide ions has been thoroughly investigated in previous work.[28] Assuming complete dissociation of the anions from protons due to the low pK_a of HBr, the equilibria can be written as

$$\text{Br}^- + \text{Br}_2 \overset{K_{\text{Br}_3^-}}{\leftrightarrow} \text{Br}_3^-, \, K_{\text{Br}_3^-} = \frac{[\text{Br}_3^-]}{[\text{Br}_2][\text{Br}^-]} \qquad (13)$$

$$\text{Br}^- + 2\text{Br}_2 \overset{K_{\text{Br}_5^-}}{\leftrightarrow} \text{Br}_5^-, \, K_{\text{Br}_5^-} = \frac{[\text{Br}_5^-]}{[\text{Br}_2]^2[\text{Br}^-]} \qquad (14)$$

Similar to the quinhydrone equilibrium eqn (5), we use K to represent the activity-coefficient corrected equilibrium constant. The bromine/bromide redox potential, which is the positive terminal voltage of the QBFB, can be calculated based on the Nernst equation

$$E_{\text{pos}} = E_{\text{Br}}^{0'} + \frac{RT}{nF}\ln\left(\frac{\text{Br}_2}{[\text{Br}^-]^2}\right) \qquad (15)$$

In the following analysis, we again start with the dilute solution assumption. Therefore, $K_{\text{Br}_3^-}$ and $K_{\text{Br}_5^-}$ are taken directly from dilute solution measurements to be 16.7 and 40 respectively. The formal potential, $E_{\text{Br}}^{0'}$, defined by the measured positive half-cell potential when $[\text{Br}_2] = [\text{Br}^-]$, is found to be 1.06 ± 0.014 V and is closely approximated by the Br_2/Br^- standard potential of 1.08 V vs. SHE. In Fig. 7(a) we plot the concentration of each bromide species vs. SOC in a

solution with starting nominal concentrations of Br_2 and Br^- of 0.5 and 3 M. $[\text{Br}^-]$ decreases sharply with the cell SOC, which is still defined by eqn (7) given a 1 : 1.2 negolyte to posolyte volume ratio. $[\text{Br}_3^-]$ rises and then peaks at around 80% SOC, after which $[\text{Br}_2]$ increases noticeably.

In addition to the difference between E_{neg} and E_{pos}, a junction potential E_{junc} (or often called Donnan potential) across the ion selective Nafion membrane needs to be considered in the full-cell OCV calculation. Because protons are the dominating charge carriers, this potential can be estimated as

$$E_{\text{junc}} = \frac{RT}{F}\ln\left(\frac{\text{H}_{\text{neg}}^+}{\text{H}_{\text{pos}}^+}\right) \qquad (16)$$

The largest value of which is 10 mV for 1 M quinone at 100% SOC. The overall cell voltage therefore is

$$E_{\text{cell}} = E_{\text{pos}} - E_{\text{neg}} + E_{\text{junc}} \qquad (17)$$

E_{cell} measured in a full-cell test is plotted as black dots in Fig. 7(b) together with values calculated from eqn (17). The blue line represents the full-cell potential without accounting for complexation, the orange line includes the bromide complexation only, and the green line incorporates both bromide and quinone complexation. Similar to our earlier results in the case of half-cell potential, the measured full-cell voltage deviates from the prediction of the Nernst equation based on the unbound monomer species concentration, whereas considering the chemical equilibria of the two electrolytes significantly improves the accuracy of the analytical solution.

The general pattern of the effect that complexation has on voltages is redistributing sharp voltage changes at low and high SOC toward intermediate SOCs, resulting in more uniform voltage change over the whole SOC range. This effect occurs because all complexation species incorporate the discharged and charged species, thereby limiting their relative concentration changes at low and high SOCs. This phenomenon also persists for other flow battery chemistries, e.g. in the posolyte of vanadium RFBs.[29] The vanadium complex is found to significantly affect the electrolyte composition measurements via UV-Vis spectrophotometry, but we are aware of no discussion about its impact on cell voltage. This may be because the low value of the equilibrium constant does not cause the voltage to deviate noticeably from theoretical values based on the unbound monomer electrolyte composition.[17] However, it is likely that stronger association could occur with other flow battery chemistries, or even in vanadium systems with a different anionic species.

Conclusion

In this work, we show how quinone (Q) and hydroquinone (HQ) absolute and relative species concentration can be determined by UV-Vis spectrophotometry assuming a linear combination of molar attenuation based on the Beer–Lambert law. The formation of a third species, quinhydrone (QHQ), from the dimerization of Q and HQ, is directly observed by UV-Vis spectrophotometry; the QHQ molar attenuation coefficient is
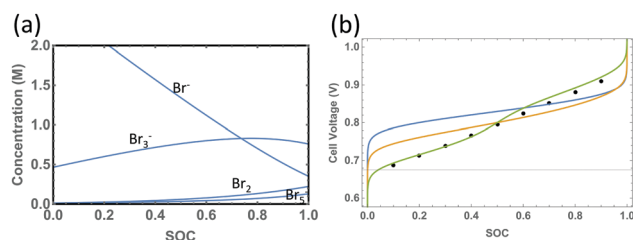

Fig. 7 QBFB full cell. (a) Posolyte speciation with $[\text{HBr}]_0 = 3$ M and $[\text{Br}_2]_0 = 0.5$ M by SOC; (b) the same posolyte against a 1.0 M $[\text{Q}]_0$ negolyte full-cell OCV vs. SOC. Black dots are experimental data. The blue line represents the OCV by the Nernst equation without any species complexation. The orange incorporates tri- and pentabromide complexation only, and green incorporates tri- and pentabromide complexation in addition to quinhydrone dimer formation. It is clear that both posolyte and negolyte complexation are critical for accurate predictions of the full-cell OCV.

measured and equilibrium constant calculated to be $K_{QHQ} \sim$ 80 M^{-1}. At high concentrations, quinone activity measurably decreases, which we tentatively interpret as a result of higher order molecular interactions. Using this value of the equilibrium constant and concentration-dependent change in redox activity based on predictions of the Nernst equation assuming an unbound monomer species concentrations and ideal solution behavior, a more accurate redox potential model is made for this electrolyte as is demonstrated by the half-cell and full-cell redox potential measurements of a quinone–bromine flow battery (QBFB).

This work enables the monitoring of quinone-based flow battery SOC *in operando* with UV-Vis spectrophotometry, and provides a framework for interpreting voltage behavior that deviates from predictions assuming ideal solution behavior in electrolytes prone to species complexation. A deeper understanding of species complexation in flow batteries not only provides insights for electrolyte optical or electrochemical behavior, but also opens the opportunity to further evaluate physical phenomena relevant to flow battery operation. Ultimately this insight can unveil pathways to improve flow battery electrolyte and hardware engineering to address the increasing demand for large-scale energy storage.

Conflicts of interest

M. J. A. is a shareholder in Green Energy Storage, S.r.l., which holds a license from Harvard University to commercialize this technology.

Acknowledgements

Notes and references

1 A. Y. Andreyev, Y. E. Kushnareva and A. A. Starkov, *J. Biochem.*, 2005, **70**, 200–214.

2 C. H. Foyer and G. Noctor, *Antioxid. Redox Signaling*, 2009, **11**, 862–878.

3 C. Costentin, *Chem. Rev.*, 2008, **108**, 2145–2179.

4 M. Yao, H. Senoh, S. I. Yamazaki, Z. Siroma, T. Sakai and K. Yasuda, *J. Power Sources*, 2010, **195**, 8336–8340.

5 Y. Liang, Y. Jing, S. Gheytani, K.-Y. Lee, P. Liu, A. Facchetti and Y. Yao, *Nat. Mater.*, 2017, **16**, 841–848.

6 B. Huskinson, M. P. Marshak, C. Suh, S. Er, M. R. Gerhardt, C. J. Galvin, X. Chen, A. Aspuru-Guzik, R. G. Gordon and M. J. Aziz, *Nature*, 2014, **505**, 195–198.

7 B. Huskinson, J. Rugolo, S. K. Mondal and M. J. Aziz, *Energy Environ. Sci.*, 2012, **5**, 8690.

8 L. Tan, H. Chen, D. Pan and N. Pan, *Eur. Polym. J.*, 2009, **45**, 1617–1624.

9 Y. Ding, Y. Li and G. Yu, *Chem*, 2016, **1**, 790–801.

10 K. Lin, Q. Chen, M. R. Gerhardt, L. Tong, S. B. Kim, L. Eisenach, A. W. Valle, D. Hardee, R. G. Gordon, M. J. Aziz and M. P. Marshak, *Science*, 2015, **349**, 1529–1532.

11 M. J. A. Qing Chen, Michael R. Gerhardt and Lauren Hartle, *J. Electrochem. Soc.*, 2016, **163**, A5010–A5013.

12 M. J. G. Moa, M. Mandado and R. A. Mosquera, *J. Phys. Chem. A*, 2007, **111**, 1998–2001.

13 V. Barone, I. Cacelli, O. Crescenzi, M. D'Ischia, A. Ferretti, G. Prampolini and G. Villani, *RSC Adv.*, 2014, **4**, 876.

14 T. J. Carney, S. J. Collins, J. S. Moore and F. R. Brushett, *Chem. Mater.*, 2017, **29**, 4801–4810.

15 E. Biilmann, *Ann. Chim.*, 1921, **16**, 321–340.

16 W. Zhang, L. Liu and L. Liu, *RSC Adv.*, 2015, **5**, 100235–100243.

17 D. N. Buckley, X. Gao, R. P. Lynch, N. Quill and M. J. Leahy, *J. Electrochem. Soc.*, 2014, **161**, A524–A534.

18 A. D. Becke, *J. Chem. Phys.*, 1993, **98**, 5648–5652.

19 S. Grimme, J. Antony, S. Ehrlich and H. Krieg, *J. Chem. Phys.*, 2010, **132**(154104), 1–19.

20 J.-D. Chai and M. Head-Gordon, *Phys. Chem. Chem. Phys.*, 2008, **10**, 6615.

21 V. Barone and M. Cossi, *J. Phys. Chem. A*, 1998, **102**, 1995–2001.

22 M. Cossi, N. Rega, G. Scalmani and V. Barone, *J. Comput. Chem.*, 2003, **24**, 669–681.

23 J. R. Pliego and J. M. Riveros, *J. Phys. Chem. A*, 2001, **105**, 7241–7247.

24 Z. Liu, J. S. Wainright, W. Huang and R. F. Savinell, *Electrochim. Acta*, 2004, **49**, 923–935.

25 Q. Chen, M. R. Gerhardt and M. J. Aziz, *J. Electrochem. Soc.*, 2017, **164**, A1126–A1132.

26 U. Er, C. Suh, M. P. Marshak and A. An Aspuru-Guzik, *Chem. Sci.*, 2015, **6**, 845–1592.

27 M. J. G. Peach, P. Benfield, T. Helgaker and D. J. Tozer, *J. Chem. Phys.*, 2008, **128**(044118), 1–8.

28 R. W. Ramette and D. A. Palmer, *J. Solution Chem.*, 1986, **15**, 387–395.

29 Z. Chen and R. Naidu, *J. Chromatogr. A*, 2002, **966**, 245–251.

Physical Chemistry Chemical Physics

ARTICLE

Supplementary Information
AQDS Material Preparation

2,7-anthraquinone disulfonic acid (AQDS)) disodium salt (>97.0% HPLC) was obtained from TCI chemicals. This sodium salt of AQDS was first dissolved in deionized water and then flushed through a column containing Amberlyst® 15(H) ion exchange resin (Alfa Aesar) activated with hydrochloric acid to replace the sodium ions with protons. Details of the procedure can be found in Reference 6. This ion-exchanged AQDS is used for all of the experiments discussed in the main text.

Synthesis of the H₂AQDS disodium salt

To further validate the construction of the UV-Vis calibration curve, AQDS was chemically reduced to AQDSH$_2$. Pd/C (10% dispersion, 1.28 g, 0.1 equivalent) was added to a stirring solution of AQDS disodium salt (5.00 g, 12.1 mmol) in deionized water (10 ml) contained in schlenk tube. The schlenk tube was sealed and purged with a flow of hydrogen gas for 30 seconds, and then filled with a balloon of hydrogen gas. The reaction mixture was placed in an oil bath at 60 ^{o}C. After 18 hours, the reaction mixture was filtered under nitrogen using standard schlenk techniques. The filtrate was evacuated to dryness to afford the reduced form AQDSH$_2$ disodium salt as a brown solid (4.95 g, 11.9 mmol) in 99% yield. Full NMR spectra are shown in Figure SI2.
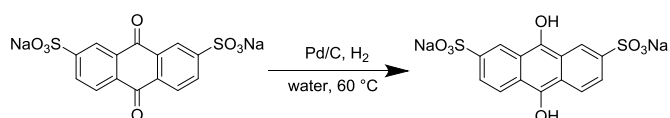

Figure SI1: Chemical reduction of AQDS disodium salt

^{1}H NMR (500 MHz, DMSO-d$_6$) δ: 8.61 (s, 2H, 2 x ArC**H**), 8.23 (d, 2H, J = 8.5 Hz, 2 x ArC**H**), 7.56 (d, 2H, J = 8.5 Hz, 2 x ArC**H**).
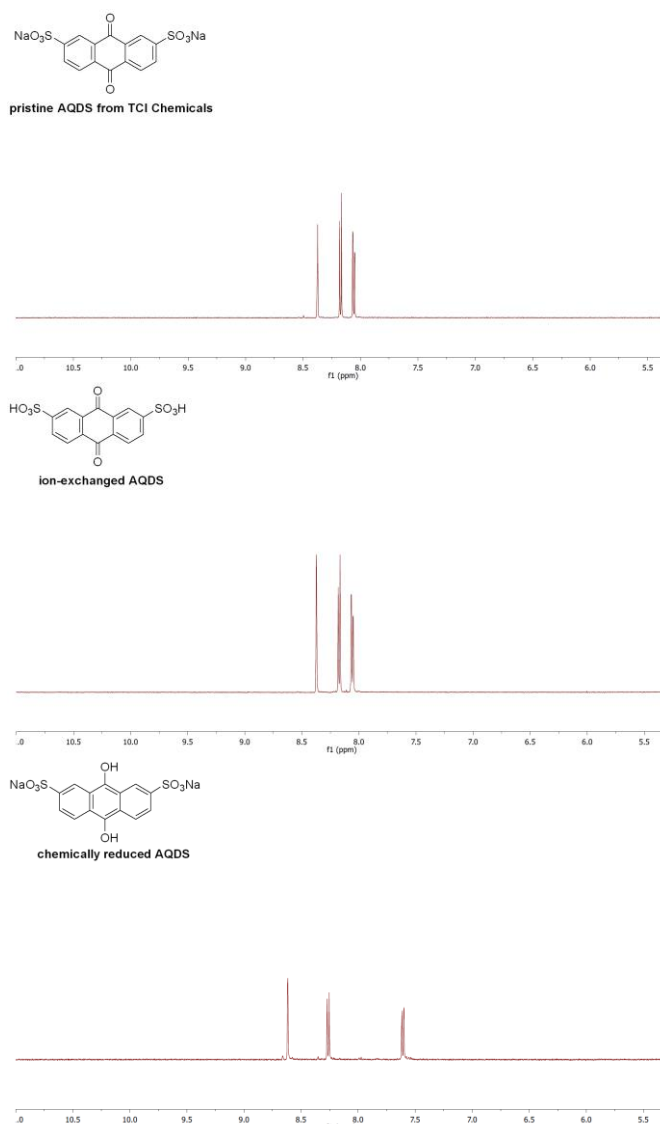

Figure SI2: NMR of (a) AQDS disodium salt, (b) ion-exchanged AQDS, and (c) H$_2$AQDS disodium salt.

UV-Vis Spectroscopy

UV-Vis spectroscopy of the chemically reduced AQDSH$_2$ disodium salt corresponds to the electrochemically reduced, ion exchanged AQDSH$_2$ described in the text as shown in Figure SI3. The sulfonate counter ion is expected to be fully dissociated and non-absorbing in the UV-Vis region. Because the chemically and electrochemically reduced AQDS have identical UV-Vis spectra and the chemically reduced AQDS NMR shows a single-species, we are confident that the electrochemically reduced AQDS calibration represents complete conversion to H$_2$AQDS (100% SOC). Full UV-Vis spectra of 1.25 mM and 209 mM AQDS are shown in Figure SI4 and Figure SI5 respectively.
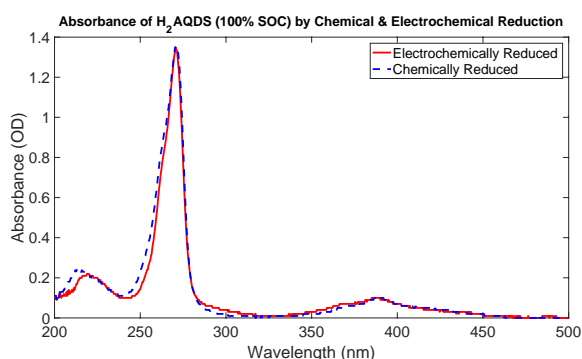

Figure SI3: Absorbance of H$_2$AQDS chemically reduced (sodium salt form) and electrochemically reduced (protonated form) to show the same, full conversion to the reduced form.
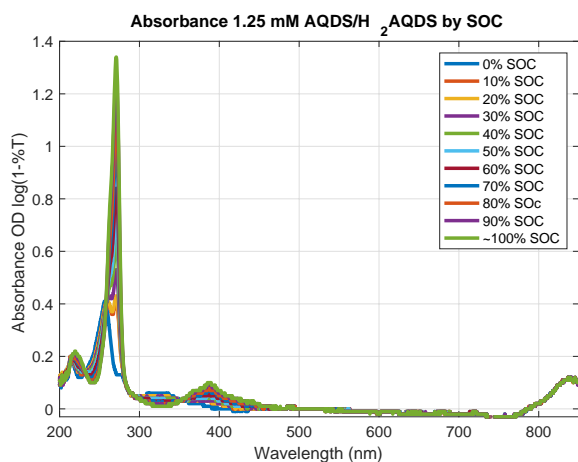

Figure SI4: Full absorbance spectrum of 1.25 M AQDS at intermediate SOCs. The absorption tail above 800 nm is expected to be a calibration artefact.
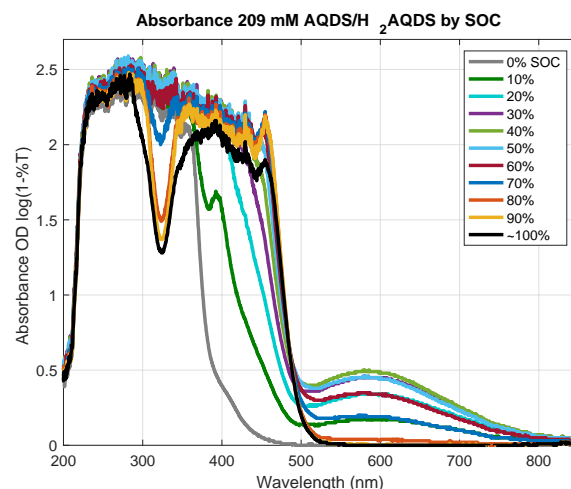

Figure SI5: Full absorbance spectrum of 209 M AQDS at intermediate SOCs. The quinhydrone dimer absorbs uniquely at wavelengths greater than 550 nm, whereas the quinone absorbs strongly in the UV, obscuring the signal in the noise.

Chronoamperometry

Full electrochemical reduction of AQDS to H$_2$AQDS was validated by chronoamperometry with over 98% of the theoretical charge accessible for a 1 M total quinone solution.
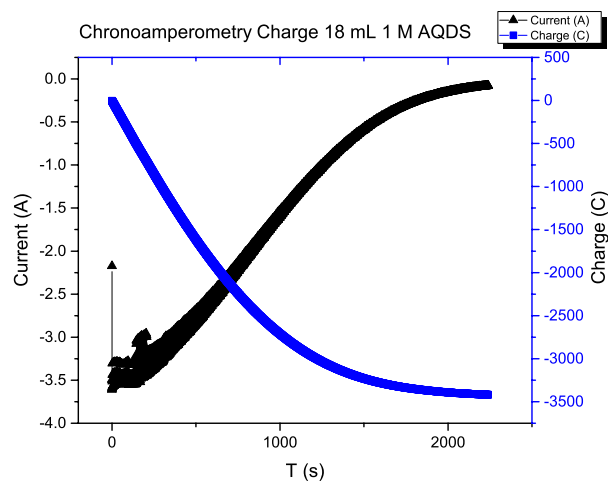

Figure SI6: The chronoamperometry curve when we reduced 18 mL of a 1 M AQDS electrolyte at -0.1 V vs. Pd-H in an AQDS-Bromide cell. 3418 C of charge were used to reduce the AQDS out of a theoretical 3473 C, representing over 98% conversion to AQDSH$_2$ (i.e. 98% SOC).

High-concentration quinone activity

In a non-flow cell as illustrated in Figure SI7, quinone activity as a function of concentration is measured via the open circuit potential (OCP) between two graphite rods placed respectively in a reference solution (10 mM Q + 10 mM HQ in 1 M H$_2$SO$_4$) and a working solution (X mM Q + 10 mM HQ in 1 M H$_2$SO$_4$) separated by

a Nafion 212 membrane. The starting quinone concentration (e.g. X = 1 M) is diluted by removing an aliquot of the working solution and replacing it with an equal volume of 10 mM HQ in 1M H_2SO_4. Relative activity coefficients correspond to the change in OCP based on deviations from ideal solution behavior.

Figure SI7(b) shows the measured OCP of the X mM Q + 10 mM HQ working electrolyte against 10 mM Q + 10 mM HQ reference electrolyte plotted on a log-linear scale where X begins at 1 M (100 [AQDS]/[H_2AQDS]) and is sequentially diluted to 100 mM (10 [AQDS]/[H_2AQDS]). The slope between 10 and 70 [AQDS]/[H_2AQDS] correlates to the expected potential based on the Nernst equation with the unbound monomer species concentrations (Equation 11) of RT/nF; the slight deviation is attributed to a small change in QHQ concentration based on the equilibrium (Equation 5) and the temporal effect of water crossover changing the liquid volume. In contrast, it is evident that this ideal solution behavior, even corrected for the unbound monomer species concentrations, is not maintained above 70 [AQDS]/[H_2AQDS], corresponding to [AQDS] > 700 mM. As is demonstrated in Figure SI7(b) the OCP plateau above 700 mM AQDS is indicative of a decrease in the activity coefficient. An example of how this could affect the negative half-cell voltage, E_{neg}, can be found as the green line in Figure 6(b) in the main text. The precise origins and quantification of this concentrated solution behavior will be discussed in future work.
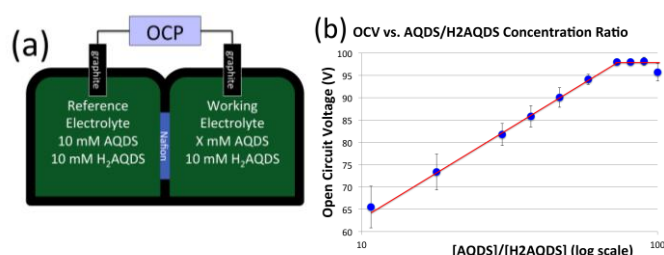

Figure SI7:(a) experimental setup for measuring quinone activity via the open circuit potential. 'X mM' indicates a starting concentration that is subsequently diluted to measure the OCP as a function of the ratio between [AQDS] and [H_2QDS] as shown in (b). It is evident that at high Q concentrations, the voltage increase ceases indicating a change in quinone activity.

Addendum to DFT calculations

There are important cost and accuracy tradeoffs in addressing the ionization of sulfonic groups in quinone-hydroquinone interaction. While it would seem more accurate to model sulfonic groups as ions, this is not the case in practicality: the accumulation of explicit charges is the system results in higher inaccuracies than modelling the protonated sites.

Whereas some or all of the sulfonic groups are ionized in solution, it is unclear how many, as their pKa is likely affected by the quinhydrone environment. In any case, ionized species do not exist as isolated ions, but as electrostatically bound ion pairs, particularly at the high ionic strengths at which the experiments were conducted. In this work, molecular configurations with ionized sulfonates balanced with hydronium ions were observed to converge, after long trajectories, to undissociated sulfonic groups.

In the anhydrous quinhydrone models we observe direct hydrogen bonding among sulfonic groups in quinone and hydroquinone, which are unphysical but they are not a consequence of the ionization degree. In the simulations where we added explicit water molecules, no interaction was observed between sulfonic groups and the opposite monomer in the quinhydrone dimer, only with the surrounding water shell. As a matter of fact, modelling ionized groups only results in increased spurious hydrogen bonding between hydroquinone and sulfonate, which the fully-solvated models confirm to be unrealistic.

The distributions of pi-stacking distances and relative angles within the ensemble of hydrated and non-hydrated hydroquinones are very similar, and less than the variance within each of the classes. The figure below shows the lack of direct hydrogen bonding within any groups in quinone or hydroquinone in the hydrated quinhydrone pair, and the large degree of hydrogen binding in the solvated sulfonic groups by explicit solvent molecules.